



# Iron oxide/carbon microsphere lithium-ion battery electrode with high capacity and good cycling stability

Meng-Yuan Li, Yan Wang, Chun-Ling Liu\*, Hao Gao, Wen-Sheng Dong\*

Key Laboratory of Applied Surface and Colloid Chemistry (SNNU), MOE, School of Chemistry and Chemical Engineering, Shaanxi Normal University, Xi'an 710062, China

## ARTICLE INFO

### Article history:

Received 27 August 2011

Received in revised form 6 February 2012

Accepted 7 February 2012

Available online 14 February 2012

### Keywords:

Lithium ion battery

Anode

Iron oxide

Carbon

Microspheres

## ABSTRACT

Iron oxide/carbon composite microspheres were prepared by a simple solution polymerization followed by pyrolysis in flowing nitrogen atmosphere at high temperature. The composites were characterized using various characterization techniques including powder X-ray diffraction, high resolution transmission electron microscopy, scanning electron microscopy,  $N_2$  physical adsorption and the electrochemical performance test. The results show that the iron oxide/carbon composites consist of uniform microspheres with an average diameter of  $\sim 2.1 \mu\text{m}$ . These iron oxide/carbon composite microspheres exhibit high capacity and good cycle stability when used as a lithium-ion battery anode. When the iron oxide content is 66%, the composite reveals the best electrochemical performance with an initial charge capacity of  $730 \text{ mAh g}^{-1}$ , and even after ninety cycles the electrode still maintains a capacity of  $664 \text{ mAh g}^{-1}$ , giving high capacity retention of 91%. The good electrochemical performance of the composite anode is close related with its structure, in which  $\text{Fe}_2\text{O}_3$  particles are uniformly dispersed in the spherical carbon matrix; hence the volume change and aggregation of the  $\text{Fe}_2\text{O}_3$  particles during lithium ion insertion/extraction process can be effectively hindered by the carbon matrix. On the other hand, carbon itself is an electronic conductor, the carbon layer and  $\text{Fe}_2\text{O}_3$  particles connect closely, which ensures a good electrical contact during lithium insertion and extraction.

© 2012 Elsevier Ltd. All rights reserved.

## 1. Introduction

Recently, transition metal oxides (MO) such as nickel oxides, cobalt oxides, tin oxides, vanadium oxides and iron oxides have been investigated as potential alternatives to carbon anode materials due to their high theoretical capacities and good safety [1–5]. Among them, iron oxides have attracted more attention due to their attractive features such as low cost, nontoxicity, and environment friendly properties. Various structures of iron oxides such as  $\text{Fe}_2\text{O}_3$  nanotubes [6],  $\text{Fe}_2\text{O}_3$  hollow microspheres [7,8], iron oxide nanowires [9],  $\text{Fe}_2\text{O}_3$  nanoflakes [10] and  $\text{Fe}_2\text{O}_3$  nanorods [11] have been employed as the anode materials of lithium ion batteries, and their electrochemical performances have been investigated.

However, there are two shortcomings limiting the applications of MO in lithium ion batteries. Firstly, MO are poor semiconductors, the low electronic conductivities of MO particles restrict the charge transfer process. Secondly, the

cyclabilities of MO electrodes are significantly affected by the volume change of MO particles. In course of lithium insertion–extraction, MO particles will pulverize into smaller particles, leading to electrical isolation of electrodes. An effective way to overcome these problems is to prepare MO/carbon composite materials, in which carbon acts as both structural buffer and conductive agent. Up to now, various iron oxides/carbon composite anode materials such as carbon-encapsulated  $\text{Fe}_2\text{O}_3$  hollow nanoparticles [12],  $\text{Fe}_2\text{O}_3$ /carbon nanocomposites [13],  $\text{Fe}_2\text{O}_3$ /Fe/carbon nanocomposites [14],  $\text{Fe}_2\text{O}_3$ /single-walled carbon nanohorns [15],  $\text{Fe}_2\text{O}_3$ /graphene [16],  $\text{Fe}_3\text{O}_4$ /graphene composite [17], and magnetite/carbon composite [18] have been prepared. Among these composites, the composite of  $\text{Fe}_2\text{O}_3$ /single-walled carbon nanohorns exhibits excellent rate performance and cycle stability [15]. However, the preparation of single-walled carbon nanohorns involved with complicated and costly apparatus, which limited its practical applications.

In the present work, we prepared iron oxide/carbon composite microspheres via a simple route using inexpensive resorcinol and formaldehyde as the carbon source. The as-prepared iron oxide/carbon composite microspheres exhibit high capacity and excellent cycle stability when used as a lithium-ion battery anode.

\* Corresponding authors. Tel.: +86 29 81530806; fax: +86 29 81530806.

E-mail addresses: [cliutt@snnu.edu.cn](mailto:cliutt@snnu.edu.cn) (C.-L. Liu), [wsdong@snnu.edu.cn](mailto:wsdong@snnu.edu.cn) (W.-S. Dong).

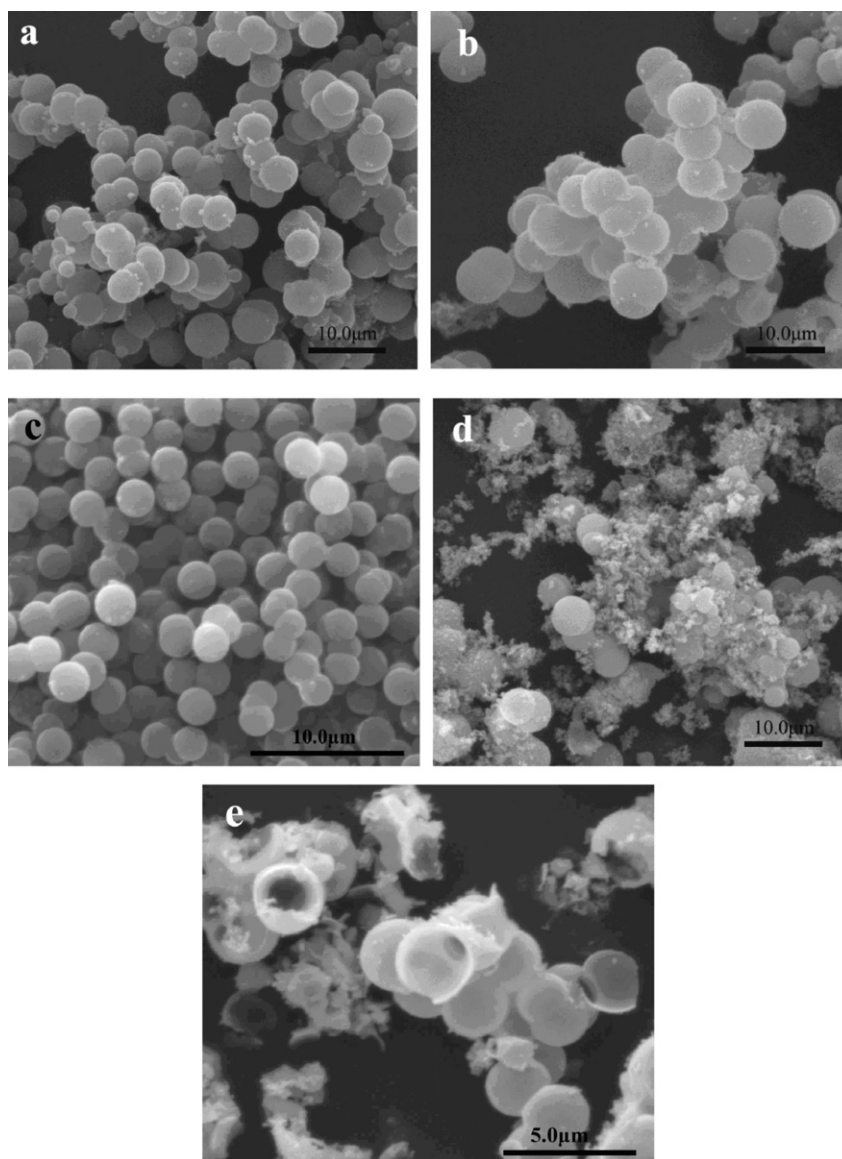


Fig. 1. SEM images of samples: (a)  $\text{Fe}_2\text{O}_3/\text{C}$ -22; (b)  $\text{Fe}_2\text{O}_3/\text{C}$ -39; (c)  $\text{Fe}_2\text{O}_3/\text{C}$ -66; (d)  $\text{Fe}_2\text{O}_3/\text{C}$ -78; and (e)  $\text{Fe}_2\text{O}_3$  hollow microspheres.

## 2. Experimental

### 2.1. Preparation of iron oxide/carbon composite microspheres and iron oxide hollow microspheres

In a typical procedure, 60 mmol of  $\text{FeCl}_3 \cdot 6\text{H}_2\text{O}$  was dissolved in 100 mL of distilled water containing 6.4 g of resorcinol and 8.6 mL of 37 wt% formaldehyde solution. The resulting mixture was then aged at  $90^\circ\text{C}$  for 3 h to produce a  $\text{FeCl}_3$ /resorcinol-formaldehyde (RF) gel composite, which was then carbonized in a tubular furnace under flowing nitrogen atmosphere via a ramping rate of  $5^\circ\text{C min}^{-1}$  from room temperature to  $600^\circ\text{C}$ , and remaining at  $600^\circ\text{C}$  for 1 h. Finally, the iron oxide/carbon composite microspheres were obtained. Based on thermogravimetric analysis (TG) analysis,  $\text{Fe}_2\text{O}_3$  content in the iron oxide/carbon composite microspheres is 66 wt%, the sample was denoted  $\text{Fe}_2\text{O}_3/\text{C}$ -66.

For comparison, the  $\text{Fe}_2\text{O}_3/\text{C}$  composites with different  $\text{Fe}_2\text{O}_3$  contents were prepared using the same procedure but with different amounts of  $\text{FeCl}_3 \cdot 6\text{H}_2\text{O}$  (20, 40, 80 mmol), the resultant samples were denoted  $\text{Fe}_2\text{O}_3/\text{C}$ -22,  $\text{Fe}_2\text{O}_3/\text{C}$ -39,  $\text{Fe}_2\text{O}_3/\text{C}$ -78,

respectively. The iron oxide hollow microspheres were prepared by calcining the sample of  $\text{Fe}_2\text{O}_3/\text{C}$ -66 at  $600^\circ\text{C}$  for 3 h in air.

### 2.2. Material characterization

Powder X-ray diffraction (XRD) was performed on a Rigaku D/MAX-III X-ray diffractometer using a  $\text{Cu K}\alpha$  source. The scanning electron microscopy and energy-dispersive analysis by X-ray (EDAX) were performed on a FEI Quanta 200. The microstructures were characterized using a high resolution transmission electron microscopy (HRTEM, JEOL JEM-2100). For the TEM analysis, a dilute suspension of the sample was dropped onto a carbon-coated TEM grid, and dried. The selected area electron diffraction (SAED) pattern was obtained using an HRTEM (JEOL JEM-2100). TG analysis was performed on a TGA Analyzer (TA-Q600SDT, USA) with a heating rate of  $10^\circ\text{C min}^{-1}$  under a flow of air. The surface area and the pore size distribution (PSD) of the samples were obtained from  $\text{N}_2$  (77 K) adsorption measurement using a Micromeritics ASAP2020 M system. The surface area of the samples was calculated by BET

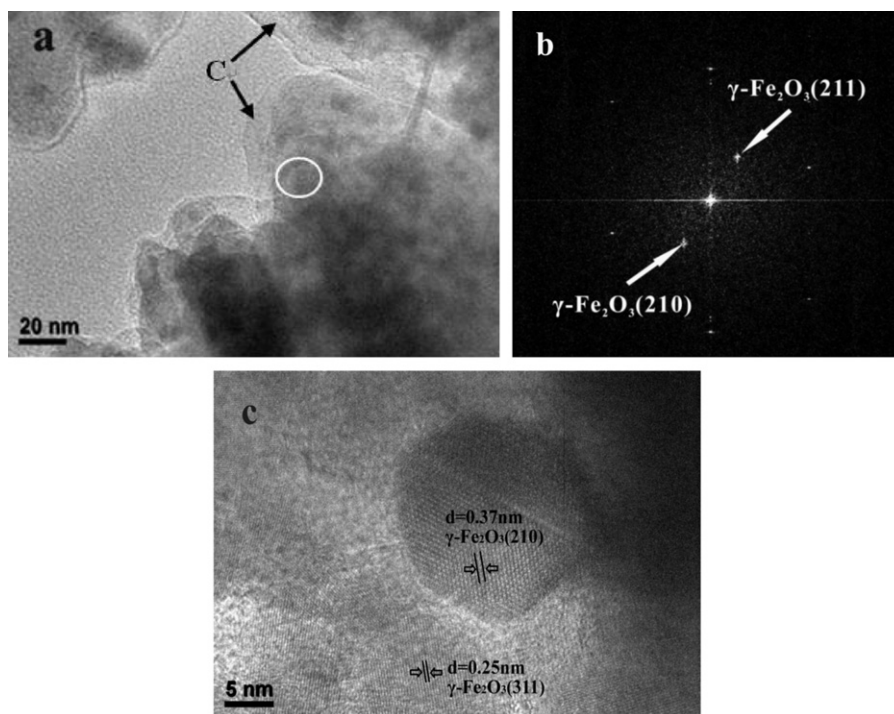


**Fig. 2.** (a) TEM images of  $\text{Fe}_2\text{O}_3/\text{C}-66$ , (b) SAED pattern for the selected region in (a), and (c) HRTEM image of  $\text{Fe}_2\text{O}_3/\text{C}-78$ .

method. The micropore surface area was obtained using the  $t$ -plot method. The average pore diameter ( $D$ ) was estimated from the  $S_{\text{BET}}$  and total pore volume ( $V$ ) according to the equation  $D = 4V/S$ .

### 2.3. Electrochemical tests

Electrochemical experiments were carried out using three-electrode lithium cells. The working electrode consists of 80 wt% active material, 10 wt% carbon black, 10 wt% polytetrafluoroethylene (PTFE). Pure lithium was used as the counter and reference electrode, and 1.0 M  $\text{LiPF}_6$  dissolved in a mixed solution of ethylene carbonate (EC)–dimethyl carbonate (DMC) (1:1, by weight) as the electrolyte. The cells (CR2032 coin type) were assembled in an argon-filled glove box. They were charged and discharged at a constant current density of  $50 \text{ mA g}^{-1}$  between cut-off potentials of 0.005 and 3.0 V on a LAND CT2001A cell test apparatus. Cyclic voltammogram (CV) experiment was performed at a scan rate of  $0.1 \text{ mV s}^{-1}$  within the range of 0–3.0 V on an electrochemistry workstation (Autolab PGSTAT302N).

## 3. Results and discussion

Fig. 1 shows SEM images of the iron oxide/carbon composites and individual iron oxide. It can be seen that  $\text{Fe}_2\text{O}_3/\text{C}-66$  is consisted of relatively uniform and well dispersed microspheres with an average diameter of  $\sim 2.1 \mu\text{m}$ . Both  $\text{Fe}_2\text{O}_3/\text{C}-22$  and  $\text{Fe}_2\text{O}_3/\text{C}-39$  are composed of microsphere aggregates.  $\text{Fe}_2\text{O}_3/\text{C}-78$  is consisted of small amounts of microspheres together with large amounts of irregular small particles. The energy dispersive analysis of X-rays (EDAX) indicates that the microspheres in  $\text{Fe}_2\text{O}_3/\text{C}-78$  contain 29.8% Fe, 25.9% O and 44.4% C; whereas, the irregular small particles contain 38.9% Fe, 31.3% O and 29.7% C.

It is known that the polycondensation of resorcinol and formaldehyde to form RF gels can be catalyzed by both acidic and basic catalysts. Acidic and basic catalysts affect differently the morphology of the produced gels at the same mass ratio (percentage of the mass of monomers to the total mass of the starting solution)

and the resorcinol-to-catalyst molar ratio [19]. The formation of the spherical structure is resulted from the shape of the RF gel, which is known to be strongly dependent on the initial pH of the reaction mixture. Micrometer-sized RF gel microspheres are known to form in the low pH conditions [20]. The initial pH values of the reaction mixtures are 0.6, 0.28, 0.15 and 0.07, respectively, during the preparation of these composites i.e.  $\text{Fe}_2\text{O}_3/\text{C}-22$ ,  $\text{Fe}_2\text{O}_3/\text{C}-39$ ,  $\text{Fe}_2\text{O}_3/\text{C}-66$  and  $\text{Fe}_2\text{O}_3/\text{C}-78$ , which led to the formation of micrometer-sized dense spherical particles containing  $\text{Fe}^{3+}$  except for  $\text{Fe}_2\text{O}_3/\text{C}-78$ . The results suggest that the content of  $\text{FeCl}_3$  also has a huge influence on the morphology of the resultant products. As presented previously, reactants tend to precipitate at very low solution pH values [19]. During the preparation of  $\text{Fe}_2\text{O}_3/\text{C}-78$ , the pH of the initial RF solution is as low as 0.07, which may cause the precipitation of some reactants; hence affects the polycondensation reaction of resorcinol and formaldehyde, resulting the formation of large amounts of irregular small particles together with small amounts of microspheres.

The iron oxide/carbon composite microspheres ( $\text{Fe}_2\text{O}_3/\text{C}-66$ ) were calcined at  $600^\circ\text{C}$  for 3 h in air, carbon in the microspheres was removed, and the oxide/carbon solid microspheres were transformed into iron oxide hollow microspheres.

The textural porosities of the synthesized samples were characterized by  $\text{N}_2$  adsorption analysis. Table 1 shows the specific surface area and pore structural parameters. It can be seen that all the samples contain a large amount of micropores. The sample  $\text{Fe}_2\text{O}_3/\text{C}-22$  has a BET surface area of  $481 \text{ m}^2 \text{ g}^{-1}$ , micropore surface area of  $425 \text{ m}^2 \text{ g}^{-1}$ , total pore volume of  $0.229 \text{ m}^3 \text{ g}^{-1}$  and micropore volume of  $0.196 \text{ m}^3 \text{ g}^{-1}$ . As the increase of  $\text{Fe}_2\text{O}_3$  in the samples, the BET surface area, micropore surface area, total pore volume, and micropore volume all decrease.

Fig. 2 shows the representative transmission electron microscopy (TEM) images of  $\text{Fe}_2\text{O}_3/\text{C}-66$  and  $\text{Fe}_2\text{O}_3/\text{C}-78$ . The samples were ground carefully using an agate mortar pestle before TEM measurement. The TEM image of  $\text{Fe}_2\text{O}_3/\text{C}-66$  (Fig. 2a) shows that there are lots of dark spots distributed well in the carbon matrix. Although the selected area electron diffraction (SAED)

**Table 1**  
Specific surface area and pore structure parameters of samples.

Samples	BET surface area (m <sup>2</sup> g <sup>-1</sup> )	Micropore surface area (m <sup>2</sup> g <sup>-1</sup> )	External surface area (m <sup>2</sup> g <sup>-1</sup> )	Total pore volume (m <sup>3</sup> g <sup>-1</sup> )	Micropore volume (m <sup>3</sup> g <sup>-1</sup> )	Average pore diameter (nm)
Fe <sub>2</sub> O <sub>3</sub> /C-22	481	425	56	0.229	0.196	4.1
Fe <sub>2</sub> O <sub>3</sub> /C-39	384	323	61	0.207	0.149	7.1
Fe <sub>2</sub> O <sub>3</sub> /C-66	202	150	52	0.143	0.069	10.6
Fe <sub>2</sub> O <sub>3</sub> /C-78	133	91	42	0.116	0.041	12.3

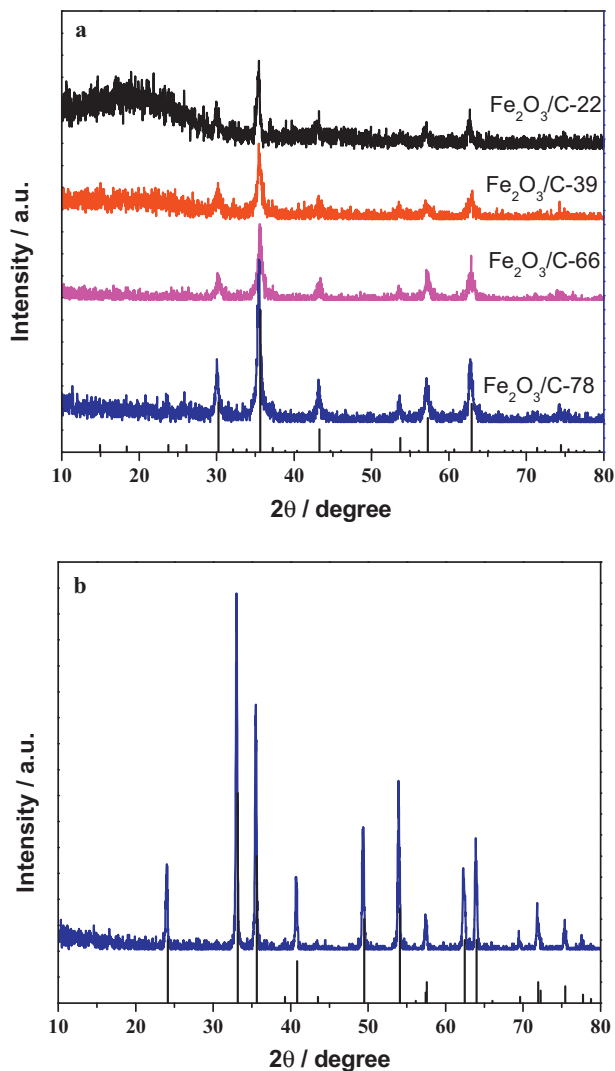


**Fig. 3.** XRD patterns of iron oxide/carbon composite microspheres (a) and iron oxide hollow microspheres (b).

pattern in Fig. 2b confirms that these dark spots are composed of  $\gamma$ -Fe<sub>2</sub>O<sub>3</sub>, no clear crystalline lattice of the dark spots is observed by HRTEM, which suggests that the surface of  $\gamma$ -Fe<sub>2</sub>O<sub>3</sub> particles would partially be covered by amorphous carbon. For Fe<sub>2</sub>O<sub>3</sub>/C-78 some  $\gamma$ -Fe<sub>2</sub>O<sub>3</sub> particles with  $\sim 20$  nm in sizes are clearly observed in the HRTEM image (Fig. 2c).

Fig. 3a shows XRD patterns of the iron oxide/carbon composites. It can be seen that all the diffraction peaks in the XRD patterns of Fe<sub>2</sub>O<sub>3</sub>/C-39, Fe<sub>2</sub>O<sub>3</sub>/C-66 and Fe<sub>2</sub>O<sub>3</sub>/C-78 can be assigned to maghemite phase of Fe<sub>2</sub>O<sub>3</sub> ( $\gamma$ -Fe<sub>2</sub>O<sub>3</sub>, JCPDS no. 39-1346). For Fe<sub>2</sub>O<sub>3</sub>/C-22, besides the peaks corresponding to the  $\gamma$ -Fe<sub>2</sub>O<sub>3</sub>, there is a broad peak at  $\sim 23^\circ$ , which is caused by the amorphous carbon in the composites. Fig. 3b shows XRD pattern of the iron oxide hollow microspheres, in which all the diffraction peaks can be well assigned to hematite phase Fe<sub>2</sub>O<sub>3</sub> ( $\alpha$ -Fe<sub>2</sub>O<sub>3</sub>, JCPDS no.

33-0664), confirming that the maghemite Fe<sub>2</sub>O<sub>3</sub> transformed into hematite phase after calcination at 600 °C for 3 h in air. The average crystalline size of Fe<sub>2</sub>O<sub>3</sub> in Fe<sub>2</sub>O<sub>3</sub>/C-22, Fe<sub>2</sub>O<sub>3</sub>/C-39, Fe<sub>2</sub>O<sub>3</sub>/C-66, Fe<sub>2</sub>O<sub>3</sub>/C-78 and Fe<sub>2</sub>O<sub>3</sub> hollow spheres calculated by Scherrer equation is about 19.7, 20.7, 19.5, 21.7 and 30.5 nm, respectively.

Fig. 4 shows the discharge/charge curves of the iron oxide/carbon composites and iron oxide hollow microsphere electrodes in the cycles. In the first discharge curves, two obvious plateaus (1.1–0.9 V and ca. 0.85 V) are clearly observed, which are similar to those of reported  $\alpha$ -Fe<sub>2</sub>O<sub>3</sub> solid nanostructures [21,6], and carbon-encapsulated Fe<sub>2</sub>O<sub>3</sub> hollow nanoparticles [12]. The plateau at 1.1–0.9 V can be ascribed to Li insertion into the Fe<sub>2</sub>O<sub>3</sub> structure, and the 0.85 V could be attributed to the reduction from Fe<sup>3+</sup> to Fe<sup>0</sup> and the formation of amorphous Li<sub>2</sub>O (Fe<sub>2</sub>O<sub>3</sub> + 6Li  $\leftrightarrow$  2Fe + 3Li<sub>2</sub>O) [12,16,6]. The 2nd and 50th discharge curves of the Fe<sub>2</sub>O<sub>3</sub>/C composites and Fe<sub>2</sub>O<sub>3</sub> hollow microspheres are different from the first, suggesting lithium-driven, structural or textural modification [17].

From Fig. 4, it can also be seen that the initial discharge capacities of Fe<sub>2</sub>O<sub>3</sub>/C-22, Fe<sub>2</sub>O<sub>3</sub>/C-39, Fe<sub>2</sub>O<sub>3</sub>/C-66, Fe<sub>2</sub>O<sub>3</sub>/C-78 and Fe<sub>2</sub>O<sub>3</sub> hollow sphere anodes are 829, 929, 1216, 1315 and 1233 mAh g<sup>-1</sup>, while the corresponding charge capacities are 362, 463, 730, 845 and 905 mAh g<sup>-1</sup>, respectively. There are large irreversible capacities in the first cycle, which leads to relatively low coulombic efficiencies of 43, 49, 60, 64 and 73%, respectively. The irreversible capacity arises most likely from the following reasons: one is the formation of solid electrolyte interface (SEI) film on the surface of tin and amorphous carbon, another is the presence of abundant unsaturated carbon atoms on these composites, which may catalyze the decomposition of electrolyte [22]. In addition, some Li ions may be permanently trapped in the carbon-matrix composites due to (a) slow Li release kinetics, (b) the formation stable lithium compounds, resulting in irreversible capacity loss or (c) strong bonding with less coordinated atoms at defect sites [23]. The first coulombic efficiencies of the samples increase gradually with increasing the contents of Fe<sub>2</sub>O<sub>3</sub> in the composites. From the second cycle, the iron oxide/carbon composite anodes and iron oxide anode deliver a charge capacity near its discharge capacity with the coulombic efficiency higher than 90%.

The electrochemical performance of the samples was investigated by CV experiments. Fig. 5 shows CV curves of Fe<sub>2</sub>O<sub>3</sub>/C-66 and the iron oxide hollow microsphere electrodes for the first three cycles. In the first cycle, Fe<sub>2</sub>O<sub>3</sub>/C-66 exhibits three peaks in the cathodic process at about 0.9, 0.6 and 0.2 V. The high intensity peak at 0.6 V can be attributed to the reduction of Fe<sup>3+</sup> to Fe<sup>0</sup>, and the peak at 0.9 V could be due to the decomposition of electrolyte, which results in the formation of an organic layer that is deposited on the surface of the particles [13,17]. The peak at 0.2 V corresponds to the insertion of Li into the carbon matrix. The peaks at 0.9 and 0.2 V disappear in the subsequent reduction process. In the anodic process, a main peak at 1.65 V and a hill at 0.3 V can be assigned to the oxidation of Fe<sup>0</sup> to Fe<sup>3+</sup> and the lithium ion extraction from carbon matrix, respectively [13]. During the subsequent cycles, the cathodic peaks at 0.6 V and anodic peak at 1.65 V are positively shifted to 0.76 and 1.8 V, respectively, indicating structural modifications in the first cycle. The CV curves of the Fe<sub>2</sub>O<sub>3</sub>/C-66 in the subsequent two cycles almost overlap, suggesting an

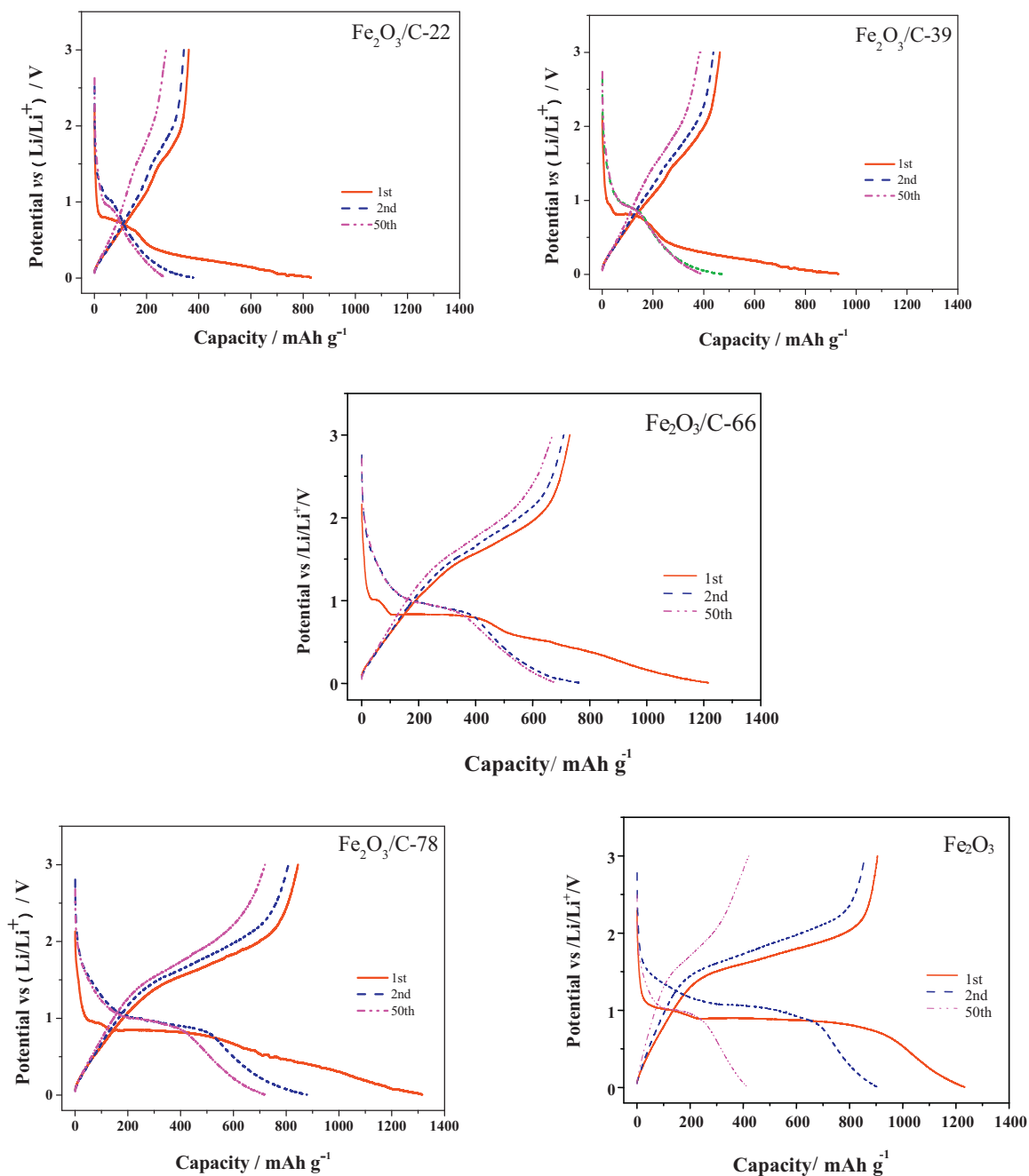


Fig. 4. The discharge/charge curves of the samples at the current density of  $50 \text{ mA g}^{-1}$ .

excellent reversibility. The iron oxide hollow microspheres electrode shows typical CV curves (Fig. 5b) which is in agreement with that reported previously [9]. In the first cycle, only a spiky peak at 0.6 V appears which corresponds to the reduction of  $\text{Fe}^{3+}$  to  $\text{Fe}^0$  in the cathodic process. The anodic peak at about 1.8 V corresponds to the reversible oxidation of  $\text{Fe}^0$  to  $\text{Fe}^{3+}$ . In the subsequent cycles, the cathodic and anodic peaks shift to 0.9 and 1.9 V, respectively.

The reversible capacity vs. cycle number profiles of the samples are illustrated in Fig. 6. It can be seen that the iron oxide anode delivers the highest initial charge capacity; however, the charge capacity of the anode decreases quickly during the subsequent cycles, after 50 cycles only shows a capacity of  $419 \text{ mAh g}^{-1}$ , which is 46% of the initial capacity. The iron oxide/carbon composite anodes show a little bit lower initial charge capacity but much better cycle stability than the iron oxide anode. Particularly,  $\text{Fe}_2\text{O}_3/\text{C-66}$  reveals

the best electrochemical performance with an initial charge capacity of  $730 \text{ mAh g}^{-1}$ , and even after ninety cycles the electrode still maintains a capacity of  $664 \text{ mAh g}^{-1}$ , giving high capacity retention of 91%.  $\text{Fe}_2\text{O}_3/\text{C-78}$  also reveals good electrochemical performance with an initial charge capacity of  $845 \text{ mAh g}^{-1}$ , and the capacity retention of 85.2% after fifty cycles.

To investigate the rate performance of the  $\text{Fe}_2\text{O}_3/\text{C-66}$  and  $\text{Fe}_2\text{O}_3/\text{C-78}$  composites, cells were cycled at various rates. Fig. 7 shows capacity vs. cycle number profiles of the samples at various current densities from 100 to  $1000 \text{ mAh g}^{-1}$ . The reversible capacity decreases slowly with increasing current density. At  $100 \text{ mA g}^{-1}$  the  $\text{Fe}_2\text{O}_3/\text{C-66}$  and  $\text{Fe}_2\text{O}_3/\text{C-78}$  composite anodes deliver a specific capacity of 606.5 and  $821.5 \text{ mAh g}^{-1}$ , respectively. At a high rate of  $1000 \text{ mA g}^{-1}$ , the specific capacity was decreased to 97.1 for  $\text{Fe}_2\text{O}_3/\text{C-66}$  and  $78.9 \text{ mAh g}^{-1}$  for  $\text{Fe}_2\text{O}_3/\text{C-78}$ . However, when the



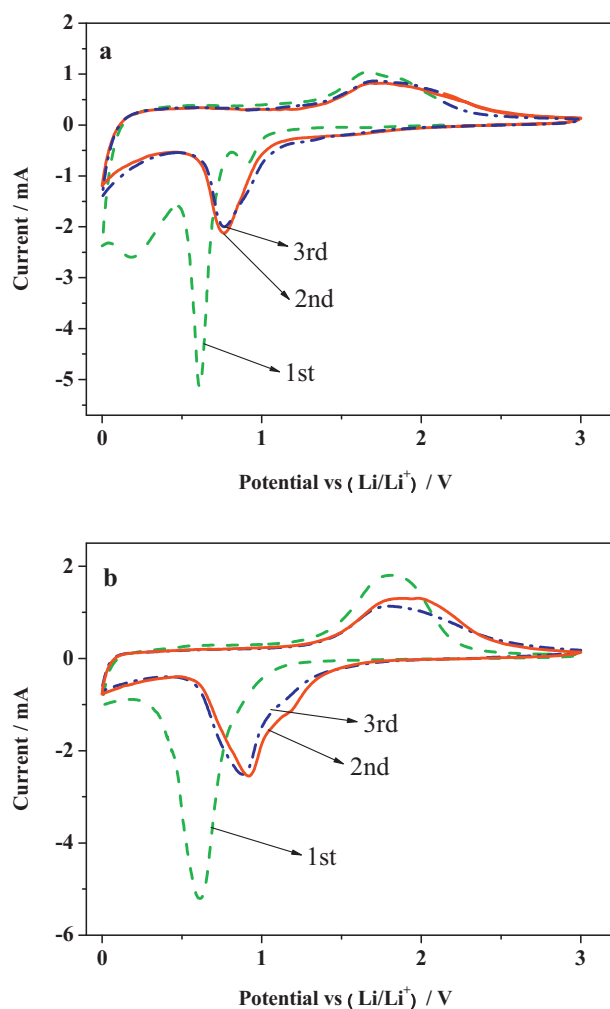


Fig. 5. CV curves of Fe<sub>2</sub>O<sub>3</sub>/C-66 microspheres (a), and iron oxide hollow microspheres (b).

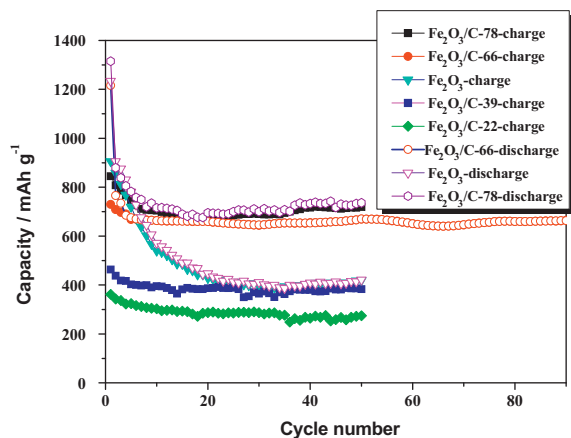


Fig. 6. Cycling performance of the samples at the current density of 50 mA g<sup>-1</sup>.

current density reduced back to 100 mA g<sup>-1</sup>, a reversible capacity of 482.0 mAh g<sup>-1</sup> for Fe<sub>2</sub>O<sub>3</sub>/C-66 and 487.9 mAh g<sup>-1</sup> for Fe<sub>2</sub>O<sub>3</sub>/C-78 could be resumed and remained stable in the following cycles. These results indicate that the Fe<sub>2</sub>O<sub>3</sub>/C-66 anode has better cycling stability than the Fe<sub>2</sub>O<sub>3</sub>/C-78. This is mainly resulted from the structural difference between Fe<sub>2</sub>O<sub>3</sub>/C-66 and Fe<sub>2</sub>O<sub>3</sub>/C-78. In the Fe<sub>2</sub>O<sub>3</sub>/C-66 composite Fe<sub>2</sub>O<sub>3</sub> particles are uniformly dispersed in

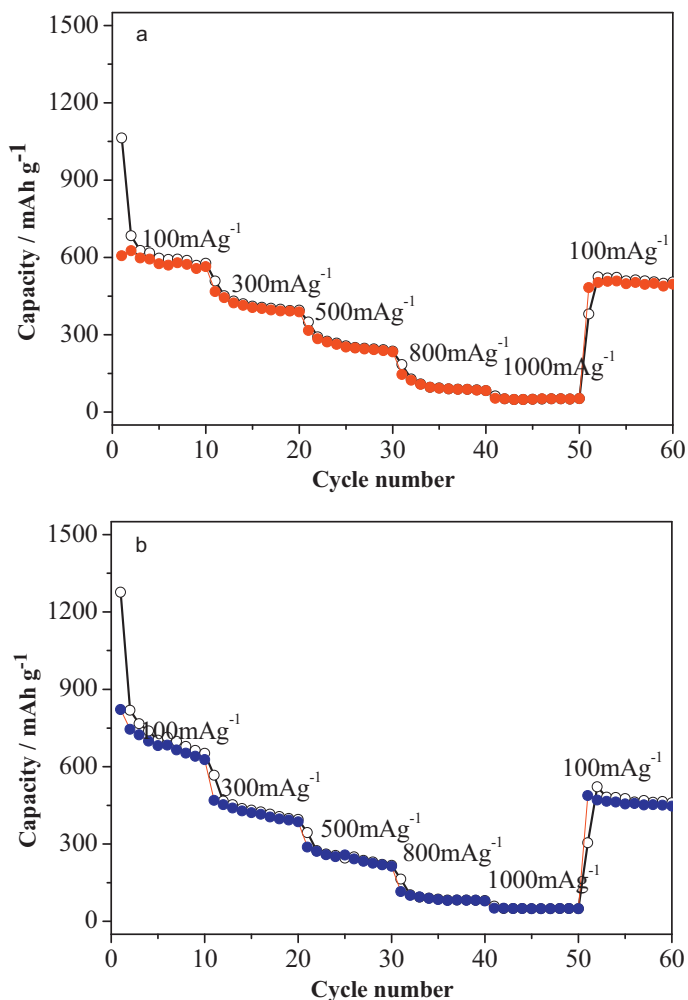


Fig. 7. Cycling performance of the Fe<sub>2</sub>O<sub>3</sub>/C-66 and Fe<sub>2</sub>O<sub>3</sub>/C-78 anodes at various current densities.

the spherical carbon matrix; hence the volume change and aggregation of the Fe<sub>2</sub>O<sub>3</sub> particles during lithium ion insertion/extraction process can be effectively hindered by the carbon matrix. On the other hand, carbon itself is an electronic conductor, the carbon layer and Fe<sub>2</sub>O<sub>3</sub> particles connect closely, which ensures a good electrical contact during lithium insertion and extraction. The Fe<sub>2</sub>O<sub>3</sub>/C-66 microsphere composite with high capacity and good cycle stability is comparable with recent results on carbon-encapsulated Fe<sub>2</sub>O<sub>3</sub> hollow nanoparticles [12], Fe<sub>2</sub>O<sub>3</sub>/Fe/carbon nanocomposites [14].

#### 4. Conclusions

Fe<sub>2</sub>O<sub>3</sub>/C composites have been prepared successfully using a simple solution polymerization route. The morphology of the resultant composites is dependent on the addition amount of ferric chloride. When the content of Fe<sub>2</sub>O<sub>3</sub> in the Fe<sub>2</sub>O<sub>3</sub>/C composites is lower than 66%, the samples are composed of microsphere or microsphere aggregates. Whereas, Fe<sub>2</sub>O<sub>3</sub>/C-78 with 78% Fe<sub>2</sub>O<sub>3</sub> is consisted of small amounts of microspheres together with large amounts of irregular small particles. XRD confirms that Fe<sub>2</sub>O<sub>3</sub> in these composites can be assigned to  $\gamma$ -Fe<sub>2</sub>O<sub>3</sub>. Among these composites, the Fe<sub>2</sub>O<sub>3</sub>/C composite with 66% Fe<sub>2</sub>O<sub>3</sub> consisting of uniform microspheres with an average diameter of  $\sim 2.1$   $\mu$ m reveals the best electrochemical performance with an initial charge capacity of 730 mAh g<sup>-1</sup>, and even after ninety cycles the electrode still maintains a capacity of 664 mAh g<sup>-1</sup>, giving high capacity retention

of 91%. This is mainly due to the fact that  $\text{Fe}_2\text{O}_3$  particles are uniformly dispersed in the spherical carbon matrix; hence the volume change and aggregation of the  $\text{Fe}_2\text{O}_3$  particles during lithium ion insertion/extraction process can be effectively hindered by the carbon matrix; hence the cracking or pulverization of the electrode is avoided.

## Acknowledgments

This work was financially supported by the Fundamental Research Funds for the Central Universities (no. GK200901002) and the Program for Changjiang Scholars and Innovative Research Team in University of China (IRT1070).

## References

- [1] P. Poizot, S. Laruelle, S. Grugeon, L. Dupont, J.M. Tarascon, *Nature* 407 (2000) 496.
- [2] B. Scrosati, *Electrochim. Acta* 45 (2000) 2461.
- [3] M. Armand, J.M. Tarascon, *Nature* 451 (2008) 652.
- [4] S. Laruelle, S. Grugeon, P. Poizot, M. Dolle, L. Dupont, J.M. Tarascon, *J. Electrochem. Soc.* 149 (2002) A627.
- [5] X.H. Huang, C.B. Wang, S.Y. Zhang, F. Zhou, *Electrochim. Acta* 56 (2010) 6752.
- [6] J. Chen, L. Xu, W. Li, X. Gou, *Adv. Mater.* 17 (2005) 582.
- [7] S. Zeng, K. Tang, T. Li, Z. Liang, D. Wang, Y. Wang, W. Zhou, *J. Phys. Chem. C* 111 (2007) 10217.
- [8] Z. Wu, K. Yu, S. Zhang, Y. Xie, *J. Phys. Chem. C* 112 (2008) 11307.
- [9] H. Liu, D. Wexler, G. Wang, *J. Alloys Compd.* 487 (2009) L24.
- [10] M.V. Reddy, T. Yu, C.H. Sow, Z.X. Shen, C.T. Lim, G.V.S. Rao, B.V.R. Chowdari, *Adv. Funct. Mater.* 17 (2007) 2792.
- [11] C. Wu, P. Yin, X. Zhou, C.O. Yang, Y. Xie, *J. Phys. Chem. B* 110 (2006) 17806.
- [12] J. Zhou, H. Song, X. Chen, L. Zhi, S. Yang, J. Huo, W. Yang, *Chem. Mater.* 21 (2009) 2935.
- [13] M.F. Hassan, M.M. Rahman, Z.P. Guo, Z.X. Chen, H.K. Liu, *Electrochim. Acta* 55 (2010) 5006.
- [14] J. Kim, M.K. Chung, B.H. Ka, J.H. Ku, S. Park, J. Ryu, S.M. Oh, *J. Electrochem. Soc.* 157 (2010) A412.
- [15] Y. Zhao, J. Li, Y. Ding, L. Guan, *Chem. Commun.* 47 (2011) 7416.
- [16] X. Zhu, Y. Zhu, S. Murali, M.D. Stoller, R.S. Ruoff, *ACS Nano* 5 (2011) 3333.
- [17] P. Lian, X. Zhu, H. Xiang, Z. Li, W. Yang, H. Wang, *Electrochim. Acta* 56 (2010) 834.
- [18] Y. Piao, H.S. Kim, Y.E. Sung, T. Hyeon, *Chem. Commun.* 46 (2010) 118.
- [19] A.M. Elkhayat, A.A. Al-Muhtaseb, *Adv. Mater.* 23 (2011) 2887.
- [20] S. Han, B. Jang, T. Kim, S.M. Oh, T. Hayeon, *Adv. Funct. Mater.* 15 (2005) 1845.
- [21] D. Larcher, C. Masquelier, D. Bonnin, Y. Chabre, V. Masson, J.-B. Leriche, J.-M. Tarascon, *J. Electrochem. Soc.* 150 (2003) A133.
- [22] Z. Chen, J. Qian, X. Ai, Y. Cao, H. Yang, *J. Power Sources* 189 (2009) 730.
- [23] W.-J. Zhang, *J. Power Sources* 196 (2011) 13.